Compensation of distant phase-distorting layers. I. Narrow-field-of-view adaptive receiver system

Miao Yu

Intelligent Optics Laboratory, Institute for Systems Research, University of Maryland, College Park, Maryland 20742

Mikhail A. Vorontsov

Intelligent Optics Laboratory, Computational and Information Sciences Directorate, U. S. Army Research Laboratory, Adelphi, Maryland 20783, and Intelligent Optics Laboratory, Institute for Systems Research, University of Maryland, College Park, Maryland 20742

Received October 24, 2003; revised manuscript received March 18, 2004; accepted April 15, 2004

We analyze various scenarios of adaptive wave-front phase-aberration correction in optical-receiver-type systems when inhomogeneties of the wave propagation medium are either distributed along the propagation path or localized in a few thin layers remotely located from the receiver telescope pupil. Phase-aberration compensation is performed with closed-loop control architectures based on decoupled stochastic parallel gradient descent, stochastic parallel gradient descent, and phase conjugation control algorithms. Both receiver system aperture diffraction effects and the effect of wave-front corrector position on phase-aberration compensation efficiency are analyzed. © 2004 Optical Society of America

OCIS codes: 010.1080, 110.0110.

1. INTRODUCTION

The primary idea of adaptive phase-distortion correction is based on the assumption that the influence of optical inhomogeneties along the optical wave propagation path can be accounted for by using an "equivalent" thin phase-distorting layer (phase screen) located at the receiver telescope pupil plane (pupil-plane phase screen).[1,2] This assumption is adequate for a number of applications including ground-based narrow-field-of-view astronomical observations, confocal microscopy, and retinal imaging.[3–6] The pupil-plane phase-screen model evokes the most well-known compensation strategy, often referred to as phase conjugation. In general terms, the phase-conjugation control rule can be expressed by the following simple formula: $u(\mathbf{r}, t) = -\varphi_p(\mathbf{r}, t)$, where $u(\mathbf{r}, t)$ is the phase correction and $\varphi_p(\mathbf{r}, t)$ is the pupil-plane phase perturbation (phase distortion), $\mathbf{r} = \{x, y\}$ is a vector in the receiver telescope pupil plane, and t is time.

The limitations of the pupil-plane phase-screen model are well recognized and affect a number of applications, such as atmospheric imaging of extended objects (wide-field-of-view imaging), laser communication over nearly horizontal propagation paths (free-space laser communication), underwater imaging, and military laser beam propagation scenarios (directed energy applications). These limitations result in intensity fluctuations (scintillations) at the receiver telescope pupil plane that are typically accompanied by the appearance of singularities in the wave-front phase known as branch points or phase dislocations.[7–11] These effects are a result of optical wave propagation (diffraction) through a medium with spatially distributed or layered refractive-index inhomogeneties.

This departure from the classical adaptive optics compensation scenario with phase perturbations located primarily at the telescope pupil gives rise to several important issues. Among these are the validity (and efficiency) of the phase-conjugation compensation strategy when the pupil-plane phase-screen approximation fails and problems related to the practical implementation of phase-conjugation control. The specific question is, how does one proceed with the compensation of phase aberrations that have a complicated topological structure containing phase singularities that cannot be easily sensed and approximated with existing adaptive optics hardware?

Wave-front phase sensing and reconstruction under conditions of strong intensity scintillations have been studied extensively with emphasis on the development of wave-front sensing and control techniques that are robust to intensity scintillations.[12–16] Important progress has also been made in the analysis of phase singularities and in the development of reconstruction algorithms that account for their presence.[7–10] Still, phase-conjugation compensation in the presence of distant phase-distorting layers (or a volume-distorting medium) remains one of the most difficult adaptive optics problems.

The legitimacy of the phase-conjugation compensation rule for the case of distant phase perturbations can be formally preserved in the approach known as multiconjugate adaptive optics (MCAO).[17–24] The MCAO technique is based on the use of several wave-front phase correctors placed in the image planes of the corresponding phase-

distorting layers (conjugate planes). The phase-conjugation correction is applied at each of the conjugated planes in the right sequence (from the pupil plane toward the most remotely located layer). This method is based on the assumption that the phase perturbations introduced by phase-distorting layers, as well as their exact positions, are known (e.g., can be reconstructed from independent measurements). Thus the conventional MCAO technique requires tomographic analysis of optical inhomogeneties along the propagation path, which represents a separate quite-complicated problem.[25]

There are several alternatives to the phase-conjugation wave-front control strategy for use in compensating phase distortions due to distant phase-distorting layers. Among these approaches are adaptive control techniques based on direct optimization of receiver system performance metrics.[26,27] The selected performance metrics, such as the Strehl ratio or various sharpness functions, are dependent on the far-field intensity distribution of the corrected wave and can be referred to as far-field metrics.

Far-field metric optimization can be achieved by using various gradient descent techniques (multidithering,[28] sequential perturbation gradient descent,[29] stochastic parallel gradient descent[30,31]), or global optimization methods (generic optimization,[32] simulation annealing,[33] or simplex algorithms[34]). The major problem with the far-field metric optimization technique is its relatively slow convergence rate. The adaptation process convergence time increases significantly with the increase in adaptive system resolution as characterized by the number of control channels N. This can be especially harmful in the case of adaptive compensation of phase aberrations induced by distant optical inhomogeneties. Complicated topology of the pupil-plane phase aberration (2π phase cuts and branch points) may require high-resolution wave-front control, even if the phase perturbations introduced by the propagation medium are relatively smooth.

A significant improvement in the convergence rate can be achieved with the recently introduced adaptive optics technique referred to as decoupled stochastic parallel gradient descent (D-SPGD).[35] The D-SPGD closed-loop controller implements gradient descent optimization of near-field performance metrics through the use of phase-contrast-type wave-front sensors. D-SPGD adaptive wave-front control is robust with respect to intensity scintillations and can provide a rapid convergence rate even for high-resolution compensations.

This study is focused on the analysis of various adaptive wave-front phase-aberration correction scenarios in optical receiver-type systems when time-independent inhomogeneties of the wave propagation medium are either distributed along the propagation path or localized in a few thin phase-distorting layers located remotely from the receiver telescope pupil. The study is divided into two parts. Part I, represented by this paper, is devoted to the analysis of stochastic parallel gradient descent wave-front phase-compensation techniques (D-SPGD and SPGD control algorithms) in adaptive receiver systems based on a single reference wave. This corresponds to the narrow-field-of-view compensation scenario typical for laser communications, small target tracking, and a number of imaging applications. D-SPGD high-resolution feedback phase-aberration compensation is compared with conventional phase-conjugated correction. Both aperture diffraction effects and the effect of wave-front phase-corrector position on phase-aberration compensation efficiency are analyzed. In Part II, contained in the following paper (this issue), the D-SPGD control technique is expanded to include extended field-of-view closed-loop operation based on multiple reference waves.

Adaptive receiver systems with D-SPGD and SPGD controllers (schematics, components, and operational principles) are described in Section 2. Numerical models of wave propagation through the turbulent atmosphere, as well as options for controlling phase perturbations and control system parameters, are discussed in Section 3.

The efficiency of D-SPGD and SPGD adaptive compensation is analyzed in Section 4. This section begins with an analysis of pupil-plane intensity and phase fluctuations for both the case of a single distant phase-distorting layer and the case of a set of phase-distorting layers. As mentioned above, the major problems of adaptive compensation of distant phase-distorting layers are the presence of strong intensity scintillations and singularities in the wave-front phase at the receiver telescope pupil plane. The D-SPGD adaptive optics system is shown here to improve the receiver system performance, although compensation efficiency as measured by the commonly used Strehl ratio degrades rapidly either when the propagation path length between the phase-distorting layer and the telescope pupil increases or when turbulence strength increases. This degradation in receiver system performance is a consequence of the influence of two major factors: (1) a decrease in the received wave energy inside the finite aperture of the telescope and (2) intensity scintillations. Neither of these effects can be overcome by increasing the adaptive compensation spatial resolution. It is also shown that ideal (continuously distributed) phase conjugation and D-SPGD adaptive systems provide nearly the same compensation efficiency, whereas D-SPGD phase control is more efficient for low-resolution correction. Section 4 concludes with an analysis of the optimal wave-front corrector position for the case of multiple phase-distorting layers. It is shown that for a receiver telescope with finite aperture size, the optimal wave-front corrector position coincides with the conjugate pupil plane rather than the plane conjugated to the phase-distorting layer. Hence the use of multiconjugated adaptive correctors positioned in the conjugate planes of the phase-distorting layers may have no advantage over a single pupil-plane corrector with an equivalent spatial resolution.

2. ADAPTIVE RECEIVER SYSTEM WITH DECOUPLED STOCHASTIC PARALLEL GRADIENT DESCENT CONTROLLER

A. System Schematic

A schematic of the narrow-field-of-view adaptive receiver system based on the D-SPGD optimization technique considered here is shown in Fig. 1. This system consists of the following major components: (a) a wave propagation path with a set of thin, random phase-distorting layers

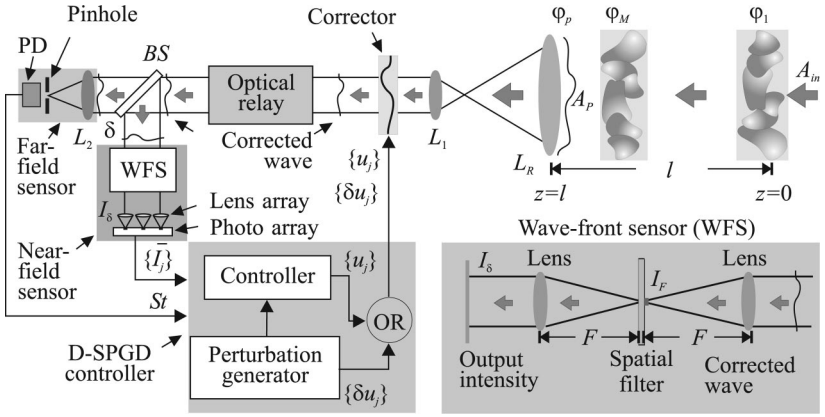

Fig. 1. Adaptive receiver system setting with distant phase-distorting layers. The closed-loop (feedback) system with a single phase corrector operates with a D-SPGD controller and two (near- and far-field) wave-front sensors. The optical relay system and the beam splitter, BS, provide simultaneous re-imaging of the wave-front corrector at the input apertures of both wave-front sensors. The schematic of the near-field wave-front sensor (PDI) is shown at the bottom right. In the adaptive system with the SPGD controller, the near-field wave-front sensor is absent. OR, logical "or."

[phase screens $\varphi_j(\mathbf{r})$, $j = 1,...,M$] equally spaced over the propagation distance l, (b) a receiver telescope (lens L_R) and lens L_1 confocal to lens L_R, (c) a wave-front corrector located in the plane conjugate to the telescope pupil (image plane of the pupil) formed by lens L_1, (d) an optical relay system that re-images the corrector aperture into two identical planes corresponding to the input planes of the wave-front sensors, (e) a near-field wave-front sensor, WFS, that includes a point-diffraction (PDI) interferometer, a lens array, and a photo array, (f) a far-field sensor (lens L_2 and a pinhole with photo detector located behind it), and (g) a D-SPGD (or SPGD) controller supplying (in sequence) to the corrector actuators the control signals $\{u_j\}$ (where $j = 1,..., N$) or the control signals that include small perturbations $\{\delta u_j\}$.

For simplicity, assume that the lens system L_R, L_1 forms an undistorted copy of the pupil-plane field $A_p(\mathbf{r}) = I_p^{1/2}(\mathbf{r})\exp[i\varphi_p(\mathbf{r})]$ scaled by the factor $M_s = 1$ at the corrector (conjugate) plane, where $I_p(\mathbf{r})$ and $\varphi_p(\mathbf{r})$ are the pupil-plane intensity and the phase, respectively. To simplify notation, we omit time dependency by assuming that optical inhomogeneties along the propagation path are fixed ("frozen").

B. Wave-Front Corrector

A rectangular array of $N = n_c \times n_c$ piston-type elements with zero spacing in between (100% fill factor) and the aperture size $D_c = n_c d_c$ is considered as the adaptive system wave-front corrector, where d_c is the element size.

The phase modulation $u(\mathbf{r}) = \Sigma_{j=1}^{N} u_j S_0(\mathbf{r} - \mathbf{r}_j)$ introduced by the corrector depends on the control signals (controls) $\{u_j\}$ and the stepwise influence functions $\{S_0(\mathbf{r} - \mathbf{r}_j)\}$ centered at the points $\{\mathbf{r}_j\}$ that coincide with the centers of the correcting elements. In most cases considered here, we assumed that the receiver telescope aperture, as well as the aperture of the re-imaging lens, is significantly larger than the corrector aperture projected to the telescope pupil plane, and hence D_c can be regarded as the receiver aperture size.

C. Wave-Front Sensors

The corrected wave with residual phase $\delta(\mathbf{r}) = u(\mathbf{r}) + \varphi_p(\mathbf{r})$ is divided by the beam splitter, BS, as shown in Fig. 1 with inputs to both the far-field and the near-field wave-front sensors. The far-field wave-front sensor provides measurements of the far-field metric $J_{f\text{-}f}$, which is proportional to the measure of optical system performance known as the Strehl ratio.[1] The Strehl ratio is given by the normalized on-axis focal plane intensity (I_F): $St = I_F/I_F^0$, where I_F^0 is the on-axis intensity in the absence of phase aberrations.

The near-field wave-front sensor is based on an optical scheme of the point-diffraction interferometer (PDI).[14,35–37] The sensor consists of two lenses with a focal distance F and an absorbing element (spatial filter) placed in the common focal plane of the lenses as shown in Fig. 1. The spatial filter has a small circular region (a dot) in the focal-plane center. The dot introduces an attenuation by a factor $\zeta_0 < 1$ applied only to the input wave zero-order spatial spectral component (on-axis focal-plane field component) $A_F(\mathbf{q} = 0)$, where $\mathbf{q}$ is a wave vector associated with the coordinate vector $\mathbf{r}_F = \lambda\mathbf{q}/F$ in the lens focal plane. We also examined the control scheme based on the optoelectronic PDI described in Ref. 15. In this sensor the attenuation ζ_0 is introduced into the input wave spectral component $\mathbf{q} = \mathbf{q}_{\max}$ corresponding to the maximum focal-plane intensity $I_F(\mathbf{q} = \mathbf{q}_{\max}) = \max I_F(\mathbf{q})$.

The near-field wave-front sensor transforms the residual wave-front phase aberration $\delta(\mathbf{r})$ in the distorted input field into the sensor output intensity $I_\delta(\mathbf{r})$, thus performing two-dimensional phase-aberration sensing. Note that the output signal of the far-field sensor measuring the far-field metric $J_{f\text{-}f}$ (the Strehl ratio) is a one-dimensional signal.

The output field of the near-field sensor is divided by the sensor's lens array into an array of $N = n_c \times n_c$ subapertures. The sensor's subapertures have exactly the same geometry as the subapertures of the phase-correcting elements, so that the jth element of the lens array collects only a portion of the optical field correspond-

ing to the jth element of the wave-front corrector. Here we ignore diffraction effects by assuming that the relay system in Fig. 1 provides ideal re-imaging of the corrector plane.

The photo-array elements collect light from the lens-array subapertures. The output signals of the photo array $\{\bar{I}_j\}$ are proportional to the wave-front sensor output intensity integrated over the subaperture areas $\{\Omega_j\}$ of the sensor:

$$\bar{I}_j = \int_{\Omega_j} I_\delta(\mathbf{r}) \mathrm{d}^2\mathbf{r}. \tag{1}$$

D. Decoupled Stochastic Parallel Gradient Descent and Stochastic Parallel Gradient Descent Controllers

The D-SPGD controller performs an iterative update of the control voltages $\{u_j^{(n)}\}$.[35] The nth step of the iteration process includes (a) measurement of the near-field wave-front sensor output signals $\{\bar{I}_j^{(n)}\}$, (b) generation of the random (pseudorandom) perturbations $\{\delta u_j^{(n)}\}$ and computation of the perturbed control signals $\{u_j^{(n)} + \delta u_j^{(n)}\}$ applied to the corrector actuators (electrodes), (c) measurement of the sensor output signals $\{\bar{I}_j^{(n+1)}\}$ corresponding to the perturbed control parameters $\{u_j^{(n)} + \delta u_j^{(n)}\}$, (d) calculation of the sensor output perturbations $\{\delta\bar{I}_j^{(n)}\} = \{\bar{I}_j^{(n+1)} - \bar{I}_j^{(n)}\}$, (e) computation of the products $\delta\bar{I}_j^{(n)}\delta u_j^{(n)}$, and (f) update of the controls in accordance with the following iterative procedure[35]:

$$u_j^{(n+1)} = u_j^{(n)} - \gamma^{(n)}\delta\bar{I}_j^{(n)}\delta u_j^{(n)}, \qquad (j = 1,...,N), \tag{2}$$

where $\gamma^{(n)} > 0$ are the update coefficients (gain coefficients).

To speed up convergence of the iterative procedure (2), the gain coefficient can be adaptively adjusted by using information obtained from the far-field sensor (e.g., the Strehl ratio). In the analysis described below, the following gain coefficient adjustment rule was applied:

$$\gamma^{(n)} = \gamma_0(1 - \kappa St^{(n)}), \tag{3}$$

where γ_0 and $0 < \kappa < 1$ are coefficients and $St^{(n)}$ is the Strehl ratio value at the nth iteration. This gain coefficient adjustment allows the gain coefficient at the beginning of the adaptation process to be large when the Strehl ratio is small and to decrease as the Strehl ratio increases, thus protecting the adaptation process from oscillatory instability in the vicinity of a metric extremum. The gain coefficient adjustment allowed approximately 25%–30% improvement in the convergence rate for all adaptation scenarios examined.

As shown in Ref. 35, iterative procedure (2) of the control signal update minimizes the near-field compensation performance metric J_3:

$$J_3 = \sum_{j=1}^{N} \bar{I}_j = \int_{\Omega_C} I_\delta(\mathbf{r}) \mathrm{d}^2\mathbf{r}, \tag{4}$$

where Ω_C is the wave-front sensor/corrector aperture area. The metric J_3 is proportional to the total light power at the wave-front sensor output. Correction of wave-front phase distortions results in concentration of the light energy near the vicinity of a single point $\mathbf{r}_F = \mathbf{r}_F^0$ in the PDI sensor focal plane. For the conventional PDI the vector $\mathbf{r}_F^0$ corresponds to the on-axis point ($\mathbf{r}_F^0 = 0$), whereas in the case of the optoelectronic PDI sensor the vector $\mathbf{r}_F^0$ is associated with the focal point that has maximum intensity: $I_F(\mathbf{r}_F^0) = \max I_F(\mathbf{r}_F)$.

Thus for both sensors, phase distortion compensation by use of the D-SPGD controller results in stronger attenuation of the wave entering the sensor due to the sensor's spatial filter. In turn, this increases the losses of the sensor's output wave energy and hence results in the minimization of the metric J_3.

The SPGD control algorithm, also examined here, utilizes the output signal of the far-field sensor $J_{f\text{-}f}$ (see Ref. 30):

$$u_j^{(n+1)} = u_j^{(n)} - \gamma^{(n)}\delta J_{f\text{-}f}^{(n)}\delta u_j^{(n)} \qquad (j = 1,...,N), \tag{5}$$

where the perturbations $\{\delta u_j^{(n)}\}$ and the gain coefficient $\gamma^{(n)}$ are the same as in the case of the D-SPGD controller (2). In contrast to the D-SPGD correction rule (2), Eq. (5) depends on the perturbed far-field metric value $\delta J_{f\text{-}f}^{(n)}$.

3. NUMERICAL MODEL OF THE ADAPTIVE RECEIVER SYSTEM

A. Propagation Equation

Assume that a monochromatic and spatially coherent on-axis reference wave (beam) with optical field complex amplitude $A_{\mathrm{in}}(\mathbf{r})$ propagates in an optically inhomogeneous medium (the atmosphere) toward an adaptive telescope receiver located a distance $z = l$ from the input plane $z = 0$ (plane of the farthest phase-distorting layer), as shown in Fig. 1. Propagation can be described by the parabolic equation for the optical field complex amplitude $A(\mathbf{r}, z)$,[38]

$$2ik\frac{\partial A}{\partial z} = \nabla_\perp^2 A + 2k^2 n_1 A, \tag{6}$$

where $\nabla_\perp^2$ is the Laplacian operator over the transversal coordinates x and y, $n_1 = n_1(\mathbf{r}, z)$ is the function describing the refractive-index fluctuations of the propagation medium along the propagation path, and $k = 2\pi/\lambda$ is the wave number.

The complex amplitude of the input (reference) wave is given by

$$A(\mathbf{r}, z = 0) = I_{\mathrm{in}}^{1/2}(\mathbf{r})\exp[i\varphi_{\mathrm{in}}(\mathbf{r})], \tag{7}$$

where $I_{\mathrm{in}}(\mathbf{r})$ and $\varphi_{\mathrm{in}}(\mathbf{r})$ are the intensity and phase distributions, respectively.

Consider the input wave intensity distribution in the form

$$I_{\mathrm{in}}(\mathbf{r}) = I_0 \exp[-(|\mathbf{r}|^2/a^2)^n], \tag{8}$$

where $n = 1$ corresponds to a Gaussian beam and $n > 1$ to a super-Gaussian beam and a is the beam width (beam radius).

The Gaussian beam is a commonly used model in the analysis of various laser beam propagation scenarios. The super-Gaussian beam model is often used to approximate in numerical simulations a plane wave that propagates from a reference light source located at infinity (e.g., a natural or laser guide star[18,39]). We assume that the

super-Gaussian beam has a diameter $2a$ exceeding the receiver telescope aperture diameter D_c. Gray-scale images of the intensity distributions superimposed on the wave-front corrector aperture area for the Gaussian ($a = D_c$) and super-Gaussian ($n = 4$ and $a = 1.5D_c$) beams used in the analysis are shown in Figs. 2a and 2b below.

B. Phase-Distorting Layers

Assume that the refractive-index inhomogeneties of the propagation medium can be modeled by a few relatively thin phase-distorting layers that principally contribute to the pupil-plane wave-front phase aberration $\varphi_p(\mathbf{r})$. For this propagation medium (layered) model, the refractive-index fluctuations in Eq. (6) can be represented in the form[4,38]

$$n_1(\mathbf{r}, z) = \sum_{j=1}^{M} \left[\delta(z - z_j) \int_{z_{j-1}}^{z_j} n_1(\mathbf{r}, z')\mathrm{d}z' \right] = -k^{-1} \sum_{j=1}^{M} [\delta(z - z_j)\varphi_j(\mathbf{r})], \quad (9)$$

where $\delta(z - z_j)$ are delta functions at the locations of the distorting layers $\{z_j\}$ $(j = 1,\ldots,M)$ and $\{\varphi_j(\mathbf{r})\}$ are the phase perturbations introduced by the phase-distorting layers.

Two models for propagation-medium inhomogeneties are considered: (a) a single phase-distorting layer ($M = 1$) placed at the plane $z = 0$ [distant phase screen $\varphi_1(\mathbf{r})$] and (b) a multilayered phase-distorting-medium model with $M = 10$ phase screens equally spaced over the distance l.

The single-layer model is important not only because it is a simple model that allows for a better understanding (in the most "pure" form) of the impact of remotely located phase distortions but also because it can be used as a first-order approximation for adaptive transmitter–receiver optical system arrangements typical of free-space laser communications and directed energy applications. In free-space laser communication applications, the pupil-plane phase screen at one of the transceiver telescope pupils is in fact a distant phase screen with respect to the second transceiver. Thus the propagation model should include at least two phase-distorting layers in such systems: the distant phase screen and the pupil-plane phase screen.

C. Phase-Perturbation Statistical Model

For phase perturbations we consider realizations of the statistically homogeneous and isotropic random function $\varphi(\mathbf{r})$ with zero mean and Andrews power spectrum[40]:

$$G_A(q) = 2\pi 0.033(1.68/r_0)^{5/3}(q^2 + q_A^2)^{-11/6} \exp(-q^2/q_a^2) \times [1 + 1.802(q/q_a) - 0.254(q/q_a)^{7/6}]. \quad (10)$$

Here r_0 is the Fried parameter,[41] and $q_A = 2\pi/l_{\mathrm{out}}$ and $q_a = 2\pi/l_{\mathrm{in}}$, where l_{out} and l_{in} are the outer and inner scales of the turbulence.

Atmospheric turbulence strength for a receiver system with aperture size D_c can be characterized by the following two parameters: the ratio D_c/r_0 and the ensemble-averaged standard deviation $\sigma_{\mathrm{ph}} = \langle \sigma_\varphi \rangle$ of the phase fluctuations inside the wave-front corrector area S. Here

$$\sigma_\varphi = \left(\frac{1}{M} \sum_{j=1}^{M} \sigma_j^2 \right)^{1/2}, \qquad \sigma_j^2 = S^{-1} \int_{\Omega_C} \varphi_j^2(\mathbf{r})\mathrm{d}^2\mathbf{r}, \quad (11)$$

and σ_j is the standard deviation of the random phase perturbations $\varphi_j(\mathbf{r})$ associated with the jth screen.

In numerical simulations, ensemble averaging was always performed over 50 realizations of the set of M phase screens. The standard deviation value σ_{ph} can be varied by changing the Fried parameter r_0 in Eq. (10).

D. Control Signal Perturbations

Spatial correlation properties of the control signal perturbations $\{\delta u_j\}$ used in both the D-SPGD (2) and SPGD (5) control algorithms may significantly affect the adaptation process convergence rate.[30,35] In the numerical analysis, the control signal perturbations $\{\delta u_j\}$ were obtained by using a decomposition of the random function realizations $\delta u(\mathbf{r})$ over the stepwise wave-front corrector influence functions $\{S_0(\mathbf{r} - \mathbf{r}_j)\}$. Similar to the results obtained in Refs. 30 and 35 for the single pupil-plane distorting layer, the best performance (convergence rate) is achieved with random realizations $\delta u(\mathbf{r})$ that are statistically matched to the phase aberrations $\varphi(\mathbf{r})$ introduced by the distorting layers, so that both random functions $\delta u(\mathbf{r})$ and $\varphi(\mathbf{r})$ have the same power spectrum (10).

With the D-SPGD algorithm, further improvement in the adaptation process convergence rate can be obtained with the use of the perturbations $\delta u(\mathbf{r})$ ("mixed" perturbations) composed of a random function realization corresponding to the atmospheric distortions $\delta u_a(\mathbf{r})$ and a component proportional to the near-field wave-front sensor output intensity $I_\delta(\mathbf{r})$: $\delta u(\mathbf{r}) = \mu \delta u_a(\mathbf{r}) + (1 - \mu) I_\delta(\mathbf{r})$, where $0 < \mu < 1$ is a weighting coefficient.[35]

E. Numerical Model Parameters

The numerical grid size used in the computer simulations contained 512×512 pixels. The wave-front corrector (receiver aperture) size D_c corresponds to the central grid area of 128×128 pixels. The phase perturbations $\varphi(\mathbf{r})$ were defined over the entire grid area (512×512 pixels), whereas the statistical characteristics of the phase fluctuations (11) were calculated only inside the corrector aperture Ω_C with the size of D_c.

In the numerical simulations, the following normalized variables were used: $\hat{\mathbf{r}} = \mathbf{r}/a$ and $\hat{l} = l/l_d$, where $l_d = 0.5ka^2$ is the diffractive length related to the input beam radius a.

4. EFFICIENCY OF NARROW-FIELD-OF-VIEW COMPENSATION

A. Pupil-Plane Intensity and Phase Fluctuations

Consider first a single distant phase-distorting layer located at the plane $z = 0$, which introduces the phase perturbation $\varphi_1(\mathbf{r})$ into the input wave. Propagation of the phase-modulated wave over the distance l to the receiver pupil plane results in the evolution of the input intensity $I_{\mathrm{in}}(\mathbf{r})$ and the phase $\varphi_1(\mathbf{r})$ into the pupil-plane intensity

$I_p(\mathbf{r})$ and phase $\varphi_p(\mathbf{r})$ fluctuation patterns. Typical examples of the development of wave intensity fluctuations (known as scintillations) and phase aberrations with an increase of the propagation distance l are illustrated in Fig. 2.

The phase modulation evolution along the propagation path results in the disappearance (filtering) of small-scale phase-aberration components, as seen in Figs. 2c–2f. This process is accompanied by the formation of the phase dislocations (branch points) and 2π phase cuts shown in Figs. 2e and 2f by arrows. The development of intensity scintillations is illustrated in Figs. 2g–2i. Small-scale intensity scintillations that occur over short propagation distances are caused by the diffraction-induced transformation of small-scale phase-modulation components into intensity fluctuations (see Figs. 2g–2i). When the propagation (diffraction) distance l increases, both the intensity scintillation amplitude and the correlation length increase.

The strength of the pupil-plane intensity scintillations can be characterized by the Rytov variance $\sigma_1^2(\mathbf{r}) = \langle I^2(\mathbf{r})\rangle/\langle I(\mathbf{r})\rangle^2 - 1$ averaged over the receiver aperture area (aperture-averaged Rytov variance),[38]

$$\sigma_I^2 = \frac{1}{S}\int_{\Omega_C} \sigma_1^2(\mathbf{r})\mathrm{d}^2\mathbf{r}, \tag{12}$$

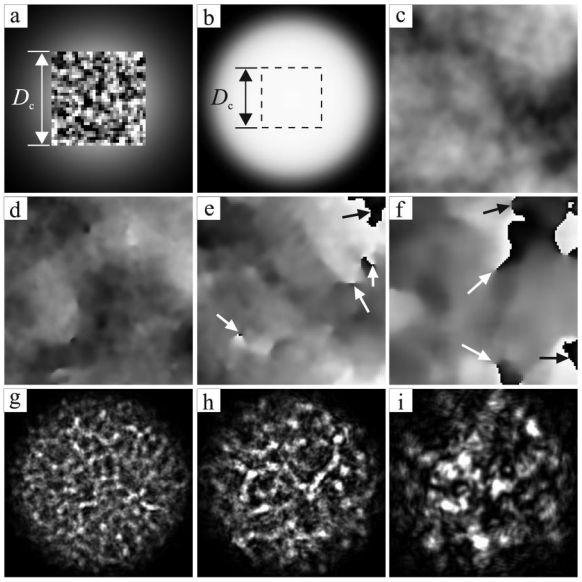

Fig. 2. Reference wave (beam) intensity and phase evolution along the atmospheric propagation path over the distance l after entering a single remote phase screen at $z = 0$. Gray-scale images of the input beam intensity for a Gaussian beam, a, and for a super-Gaussian beam, b, are superimposed on the wave-front corrector aperture. a, Random phase perturbations applied to the wave-front corrector with $N = 32 \times 32$ piston-type actuators represented by gray-scale intensity modulation. c, The remote phase-screen phase perturbation induced into the input wave at $z = 0$ ($D_c/r_0 = 3$). c–i, Evolution of phase (c–f) and intensity (b, and g–i) of the propagating super-Gaussian beam for different normalized distances $\hat{l} = l/l_d$ ($l_d = 0.5ka^2$): b and c for $\hat{l} = 0$, d and g for $\hat{l} = 0.005$, e and h for $\hat{l} = 0.01$, and f and i for $\hat{l} = 0.05$. White arrows point to the centers of phase dislocations (branch points); black arrows point to the boundaries of 2π phase cuts.

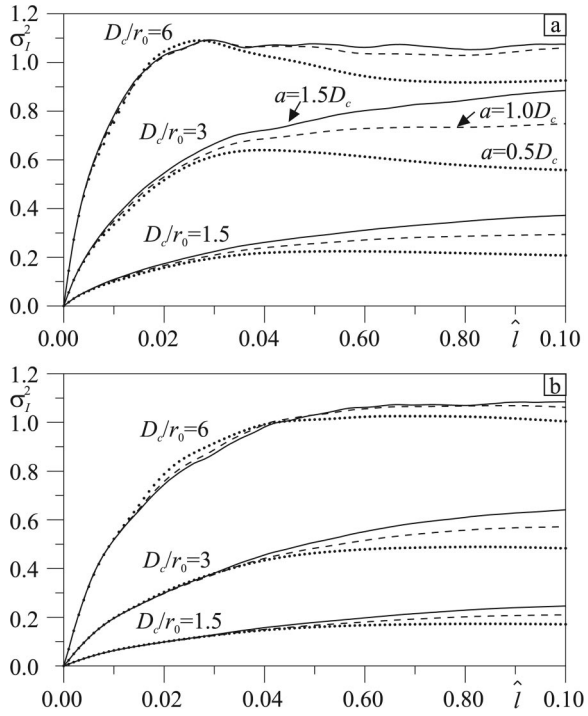

Fig. 3. Aperture-averaged Rytov variance as a function of normalized propagation distance $\hat{l} = l/l_d$: a, for a single distant phase-distorting layer and b, for ten equally spaced phase screens, with different turbulence strengths characterized by the ratios D_c/r_0. Solid curves, super-Gaussian beam with $a = 1.5D_c$; dashed and dotted curves, Gaussian beam with $a = 1.0D_c$ and with $a = 0.5D_c$, respectively.

where $\langle I(\mathbf{r})\rangle$ is the ensemble-averaged intensity distribution, and $\langle\ \rangle$ denotes ensemble averaging over a number of realizations. (In the simulations we use 50 realizations.)

Figure 3 illustrates the dependence of the variance σ_I^2 on the normalized propagation distance $\hat{l} = l/l_d$ for a super-Gaussian beam with $a = 1.5D_c$ (solid curves) and Gaussian beams with aperture radii $a = D_c$ (dashed curves) and $a = 0.5D_c$ (dotted curves). The case of a single, distant phase-distorting layer in Fig. 3a is compared in Fig. 3b with wave propagation through ten phase screens equally spaced over l and having equivalent phase-fluctuation standard deviation values σ_{ph} (or, equivalently, ratios D_c/r_0).

As seen from the curves in Fig. 3, intensity scintillations increase sharply over a relatively short propagation distance corresponding to rapid transition of the small-scale phase-distortion components into the intensity fluctuations mentioned above. When the propagation distance is increased further, intensity scintillations saturate or even decrease for a single distant phase screen (see, for example, the scintillation curves for $D_c/r_0 = 6$ in Fig. 3a). This decrease in intensity scintillations is due to diffraction-induced "smoothing" of the small-scale intensity fluctuations developed at the initial stage of the wave propagation.[42]

Note that the effects of the input beam shape (Gaussian versus super-Gaussian) and the beam width on the intensity scintillations level are less noticeable for the

multiple-layer propagation geometry in Fig. 3b. For the single phase screen in the intensity scintillation saturation regime ($l \geqslant 0.04 l_d$), the variance σ_I^2 is decidedly bigger for beams with a wider aperture.

B. Compensation Efficiency Metrics

In adaptive optics phase-aberration correction, efficiency is traditionally evaluated by using the ensemble-averaged value of the residual phase-fluctuation variance $\langle \sigma_\delta(\mathbf{r}) \rangle = \langle [\delta(\mathbf{r}) - \langle \delta(\mathbf{r}) \rangle]^2 \rangle$ (mean square phase-error metric) or its aperture-averaged value.[2] With distant phase-distorting layers, the mean square phase metric may not be able to provide an adequate compensation efficiency measure, especially for an adaptive optics technique that does not require phase reconstruction such as the D-SPGD and SPGD phase-control algorithms. Indeed, because of 2π ambiguity in the wave-front phase, there are many possible realizations of the control function $u(\mathbf{r})$ that can result in the same or nearly the same value of the optimized performance metric but that will have quite different values of the residual phase and hence different mean square phase errors.

The most adequate measure of correction efficiency for D-SPGD adaptive compensation is a metric optimized by the feedback controller. In the D-SPGD controller considered here, one such metric is the near-field metric J_3 [Eq. (4)]. On the other hand, the metric J_3 is not exactly the measure that is commonly used for analysis of optical system performance. In addition, other metrics can also be utilized in D-SPGD (or SPGD) control systems that make compensation efficiency analysis a more difficult problem. One way to circumvent this problem is to use different metrics for compensation efficiency analysis and adaptive system operation. Compensation efficiency is estimated by using the Strehl ratio, one of the most "understandable" measures of aberrations in optical systems.

C. Decoupled Stochastic Parallel Gradient Descent Convergence and Compensation Resolution

The efficiency of adaptive phase-distortion compensation depends on many factors: wave-front corrector resolution, convergence speed of the control algorithm, location of the phase-distorting layers, control system parameters, input beam type, and position of the wave-front corrector and sensor in the adaptive system optical train.

Consider first the convergence of the D-SPGD (and SPGD) compensation process and its dependence on the wave-front corrector spatial resolution and the location of the phase-distorting layer. Assume that the wave-front corrector with fixed aperture size D_c is composed of an array of $N = n_c \times n_c$ piston-type actuators, as shown in Fig. 2a. The D-SPGD system includes a PDI with the attenuation spot in an on-axis location, as in the near-field wave-front sensor described in Section 2.

Dependence of the ensemble-averaged Strehl ratio $\langle St(n) \rangle$ on the number of iterations n (adaptation evolution curves) performed by the D-SPGD controller (2) is shown in Fig. 4 for a single phase screen located either at the telescope pupil (Fig. 4a) or at a distance $l = 0.05 l_d$ from the receiver telescope (Fig. 4b). The corresponding adaptation evolution curves for ten equally spaced phase screens are presented in Fig. 4c.

In all cases considered here, the adaptation process convergence rate (defined as the number of iterations n_a required to achieve 80% of the stationary-state Strehl ratio value St_0) was between $n_a = 5$ and $n_a = 10$ for the pupil-plane phase distortions; between $n_a = 10$ and $n_a = 20$ for the single, distant phase screen; and nearly the same for multiple phase screens in Fig. 4c. The convergence rate defines the time $\tau_c = n_a \Delta\tau$ required for static phase-aberration compensation (convergence time), where $\Delta\tau$ is the time required for a single iteration. As the numerical analysis shows, convergence time in the D-SPGD system can be further decreased by nearly 10%–15% with the use of an optoelectronic PDI wave-front sensor instead of the conventional PDI with on-axis spatial filtering.

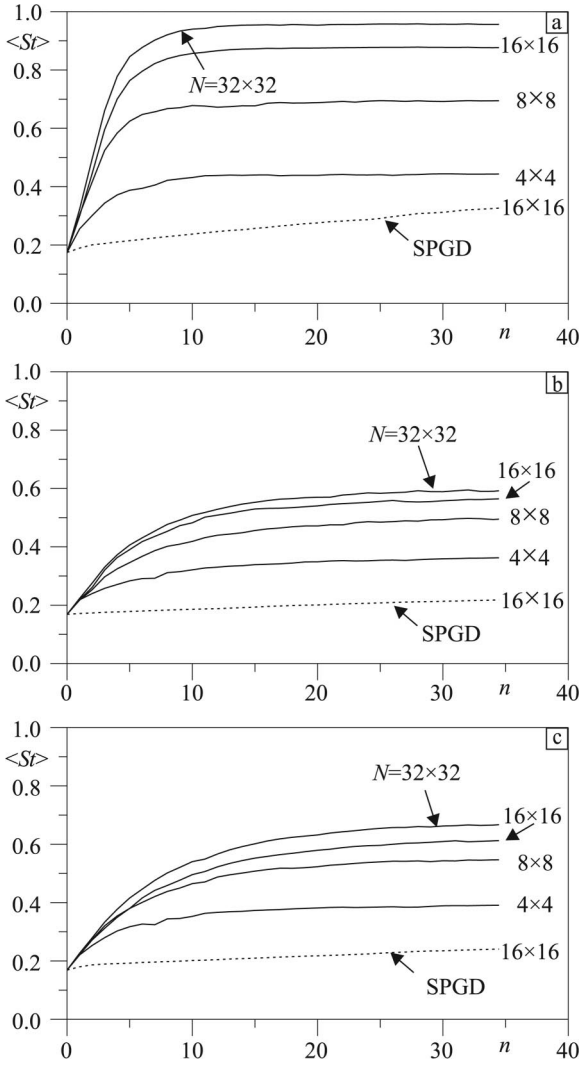

Fig. 4. Ensemble-averaged Strehl ratio adaptation curves for D-SPGD (solid curves) and SPGD (dotted curves) systems for wave-front correctors with different numbers N of piston-type correcting elements: a, single phase-distorting layer at the receiver telescope pupil; b, distant single phase-distorting layer at the distance $l = 0.05 l_d$ from the telescope pupil; and c, ten phase-distorting layers equally spaced along the distance $l = 0.05 l_d$. In all cases $D_c/r_0 = 6.0$ and the control parameters are optimized separately for each N.

For comparison, the adaptation evolution curves for the SPGD adaptive system with wave-front corrector having $N = 16 \times 16$ elements are shown in Fig. 4 by dotted lines. As expected, SPGD system operation requires a significantly longer convergence time than D-SPGD system operation. For this reason, in the following analysis we consider primarily D-SPGD closed-loop operation, which provides faster adaptation process convergence.

The fact that adaptation process convergence occurs faster for the D-SPGD system with a higher-spatial-resolution wave-front corrector is opposite to the behavior of conventional gradient descent compensation algorithms based on far-field metric optimization, for which the convergence time τ_c increases with the number of actuators (control channels) as $N^{1/2}$ or even faster.[30] The improvement in convergence speed achieved for higher-resolution compensation is due to partial decoupling of control channels obtained by using spatially distributed information from the near-field wave-front sensor.[35] Thus the D-SPGD compensation technique overcomes the main drawback of conventional gradient-descent-based adaptive optics—the rapid increase of convergence time with an increase in adaptive system resolution.

The physical reason for the relatively slow convergence for low-resolution correction ($N = 4 \times 4$ and $N = 8 \times 8$) seen in Fig. 4 is related to the computation of the sensor output signals $\{\bar{I}_j\}$ in the D-SPGD controller. The sensor outputs $\{\bar{I}_j\}$ are proportional to the wave-front sensor intensity integrated over the subaperture areas $\{\Omega_j\}$ of size d_c [see Eq. (1)]. If the subaperture size d_c exceeds the characteristic correlation radius ρ_φ of the sensor's output intensity fluctuations (which can be roughly associated with the characteristic scale of the pupil-plane phase distortions), integration over the subaperture area results in aperture averaging of the wave-front sensor information. Owing to this averaging, the sensitivity of the signals $\{\bar{I}_j\}$ with respect to the changes in the residual phase modulation decreases, which leads to a decline in adaptation process convergence speed for low-resolution corrections.

The stationary-state Strehl ratio achieved depends on the adaptive system resolution (compare in Fig. 4 the adaptation curves with different values of N) as well as on the location of the distant distorting layer (distance l). Increasing the distance l results in a decline in compensation efficiency. Note that compensation of the single distant phase-distorting layer is less efficient than the corresponding compensation of the multilayered phase perturbations (compare adaptation curves in Figs. 4b and 4c).

The properties of D-SPGD compensation mentioned above are preserved for a wide range of phase-perturbation strengths as characterized by the standard deviation of phase fluctuations σ_{ph} in Eq. (11) (or by the ratio D_c/r_0). The dependence of the Strehl ratio $\langle St \rangle$ achieved after 40 iterations on the parameter σ_{ph} for D-SPGD systems with different N is shown in Fig. 5a for the pupil-plane phase screen and in Fig. 5b for multiple distorting layers located over the distance $l = 0.05 l_d$ from the receiver telescope. The degradation in compensation efficiency for the distant phase-distorting layers is more significant for high-resolution systems (compare curves with $N = 32 \times 32$ in Figs. 5a and 5b).

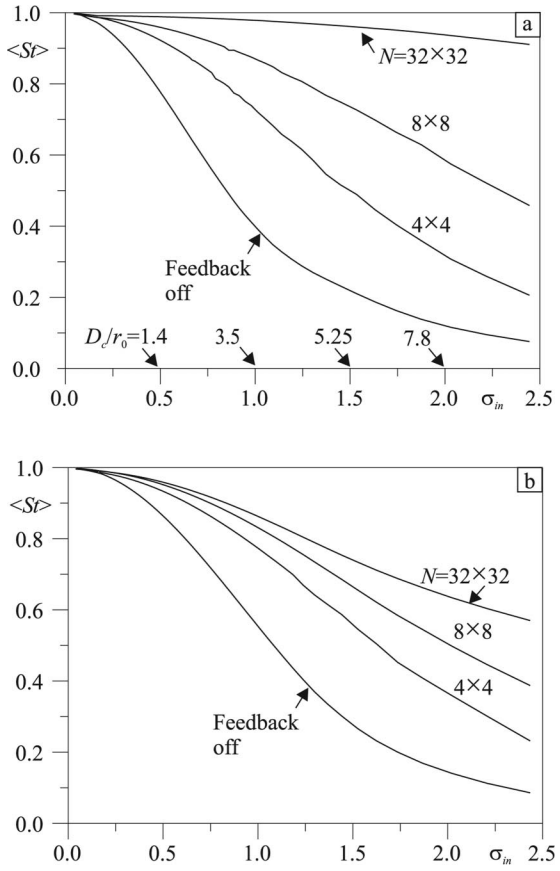

Fig. 5. Strehl ratio $\langle St \rangle$ achieved after 40 iterations of the adaptation process versus standard deviation of the phase perturbations introduced by distorting layers for the D-SPGD system with different numbers N of control elements: a, single phase-distorting layer at the pupil of the telescope; b, ten phase-distorting layers equally spaced along the distance $l = 0.05 l_d$. The control parameters are the same as in Fig. 4.

D. Compensation Efficiency for Distant Distorting Layers

Consider in more detail the effect of phase-distorting layer position (as measured by the distance l) on the efficiency of phase-distortion compensation. The corresponding Strehl ratio curves $\langle St \rangle$ are shown in Fig. 6 as functions of the normalized distance $\hat{l} = l/l_d$. As seen in Fig. 6a, when the normalized distance $\hat{l}$ is increased, the Strehl ratio decreases monotonically for both the single distant phase screen (solid curves) and the set of ten phase screens equally distributed over the distance l (multiple distorting layers). Note that in the uncompensated system, the Strehl ratio is practically independent of phase screen location (feedback-off curve in Fig. 6a).

At first glance, the Strehl ratio decline in Fig. 6a can be associated with the development of phase singularities (branch points and phase cuts) as the propagation distance l increases, which the D-SPGD system fails to compensate effectively. This suggests that some improvement in the compensation technique (higher-resolution wave-front corrector, improved control algorithm, etc.) may prevent the Strehl ratio from declining and provide better compensation performance.

E. Energy Loss Factor and Normalized Strehl Ratio

It appears that the hypothesis that topological changes in phase-aberration structure are the sole reason for decline in adaptive compensation efficiency is incorrect.

To illustrate, consider an "ideal" spatially distributed phase-conjugated correction $u(\mathbf{r}) = -\varphi_p(\mathbf{r})$ that results in zero residual phase, $\delta(\mathbf{r}) = 0$. In the numerical simulation results shown in Fig. 6b this phase conjugation correction corresponds to the wave front corrector with $N = 128 \times 128$ control channels (number of grid points inside the corrector area). As seen from the phase-conjugation correction results (dotted curves in Fig. 6b), the Strehl ratio for this ideal high-resolution correction also decreases when the propagation distance l increases. This behavior is similar to that for D-SPGD correction (solid curves in Fig. 6b). Note that the D-SPGD controller provides nearly the same Strehl ratio as does the "ideal" phase-conjugation correction.

The physical reason why the ideal phase conjugation correction of the distant phase-distorting layer does not provide an undistorted Strehl ratio value ($St = 1$) is due to several factors. First, recall that the commonly used definition of the Strehl ratio, $St = I_F/I_F^0$, includes the on-axis focal-plane intensity values for the aberrated I_F and unaberrated I_F^0 waves entering the telescope pupil. Note that both intensities depend on the received light power P inside the corrector area.

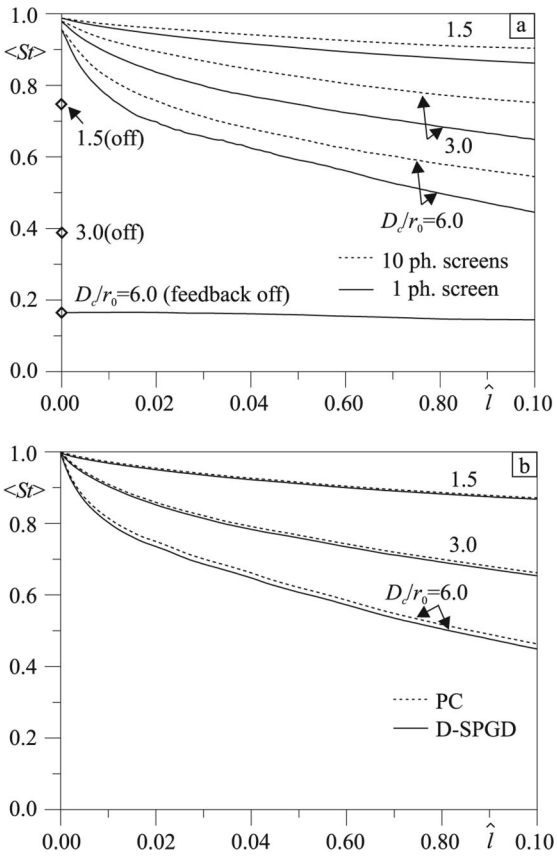

Fig. 6. Ensemble-averaged Strehl ratio $\langle St \rangle$ achieved after 40 iterations as a function of normalized propagation distance $\hat{l}$ for different D_c/r_0: a, D-SPGD system with a single distant phase screen (solid curves) and multiple distant phase screens (dotted curves); b, high-resolution D-SPGD (solid curves) and phase-conjugation (dotted curves) systems with a single distant phase screen. In a, the averaged stationary Strehl ratios before adaptation, $\langle St_0 \rangle$, are shown by diamond symbols.

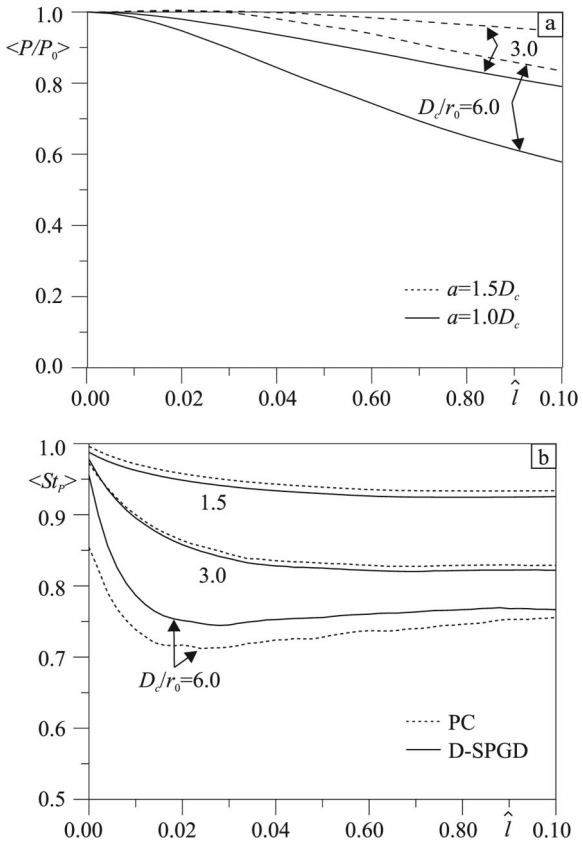

Fig. 7. Averaged energy-loss factor $\langle P/P_0 \rangle$ and the metric $\langle St_P \rangle$ (Strehl ratio $\langle St \rangle$ normalized by the energy-loss factor) for the case of a single phase-distorting layer located a distance $\hat{l}$ from the telescope pupil: a, averaged energy-loss factor $\langle P/P_0 \rangle$ for a Gaussian beam with $a = D_c$ (solid curves) and for a super-Gaussian beam with $a = 1.5D_c$ (dashed curves); b, performance metric $\langle St_P \rangle$ for the D-SPGD (solid curves) and phase conjugation systems (dotted curves) having $N = 32 \times 32$ control channels and different D_c/r_0 values.

For the pupil-plane phase screen, the received light power P is the same for both the aberrated and the unaberrated beams (pupil-plane phase distortions do not affect received power). The situation is different in compensation of distant phase-distorting layers. The phase perturbation $\varphi(\mathbf{r})$ introduced by the distorting layers increases the divergence of the laser beam and hence results in a decrease in the light power P received at the corrector area, in comparison with the unaberrated beam power P_0.

The ensemble-averaged ratio $\langle P/P_0 \rangle$ of the received power in the presence and the absence of the distant phase-distorting layers characterizes the relative energy losses at the receiver telescope caused by the beam propagation through these distant layers. In the case of the adaptive receiver system considered, the ratio $\langle P/P_0 \rangle$ depends solely on turbulence strength and propagation geometry and is not affected by the correction system. As the distance l increases, the factor $\langle P/P_0 \rangle$ decreases, as shown in Fig. 7a. This decrease in the ratio $\langle P/P_0 \rangle$ is seen to be smaller for the wider beam when one is com-

paring the energy loss factor in Fig. 7a for the input Gaussian beam with $a = D_c$ (solid curves) with the wider super-Gaussian beam with $a = 1.5D_c$ (dashed curves). Note that for the ideal plane or spherical wave, the average received power is independent of the presence of aberrations ($\langle P/P_0 \rangle = 1$).[38]

When estimating adaptive system compensation efficiency for the pupil-plane phase distortion $\varphi_p(\mathbf{r})$ originating from the distant phase perturbations, one should take these energy losses into account. This can be done by normalizing the compensation performance metric so that $St_P = (I_F/I_F^0)/(P/P_0)$—the Strehl ratio normalized by the energy-loss factor P/P_0. The metric St_P is also known as link efficiency.[43] The metric St_P corresponds to calculation of the Strehl ratio for optical waves with constant received power (independent of phase-distorting layer location). Thus the metric St_P solely characterizes the efficiency of pupil-plane phase-aberration compensation independent of the potential energy losses. At the same time, because the energy losses are typically unknown in practice, the actual measured signal by the adaptive optics system is proportional to the Strehl ratio. For this reason both metrics are considered.

F. Phase Conjugation versus Decoupled Stochastic Parallel Gradient Descent Correction

Results of the numerical analysis of adaptive system performance from using the metric $\langle St_P \rangle$ are presented in Fig. 7b for the wave-front corrector with $N = 32 \times 32$ actuators. The $\langle St_P \rangle$ metric curves are obtained for a single distorting layer located a distance l from the telescope pupil, with use of both the D-SPGD (solid curves) and the phase conjugation (dotted curves) controllers.

The dependence of the metric $\langle St_P \rangle$ on the distance l in Fig. 7b is quite different from the corresponding dependence of the Strehl ratio $\langle St \rangle$ in Fig. 6a. In contrast with the behavior of $\langle St \rangle$ in Fig. 6a, the decline in $\langle St_P \rangle$ in Fig. 7b occurs only for relatively short propagation distances $l < l_0$ ($l_0 \approx 0.02 l_d$ for $D_c/r_0 = 6$). For longer distances ($l \geqslant l_0$), efficiency of phase distortion compensation is practically independent of l. In strong turbulence conditions, the metric $\langle St_P \rangle$ actually slightly increases after the initial drop at $l < l_0$ (see curve $D_c/r_0 = 6$ in Fig. 7b). Note that the range of distances $l < l_0$ is characterized by rapid growth of the pupil-plane intensity scintillations that is due to transformation of small-scale phase aberrations into intensity fluctuations, as shown in Fig. 3.

Thus even perfect phase-conjugated compensation cannot prevent the decline in the Strehl metrics, as shown in Figs. 6b and 7b. This decline is a result of the rapid development of pupil-plane intensity scintillations, not from shortcomings in the compensation technique. When the propagation distance l increases ($l > l_0$), intensity scintillations saturate (see Fig. 3a). This corresponds to the end of the metric $\langle St_P \rangle$ decline in Fig. 7b. It follows that the continuous decline of the Strehl ratio $\langle St \rangle$ for $l > l_0$ in Fig. 6a is solely related to the energy losses mentioned above.

Now compare efficiency of phase conjugation with the D-SPGD control technique using the performance metric $\langle St_P \rangle$. As seen in Fig. 7b, for relatively strong turbulence ($D_c/r_0 = 6$), phase conjugation correction is less efficient than D-SPGD compensation. This result requires more explanation.

First, note that in simulations of the phase-conjugation correction, the phase function $\varphi_p(\mathbf{r})$ was reconstructed from the pupil-plane field complex amplitude $A_p(\mathbf{r})$ by using the ratio of the imaginary $\mathrm{Im}[A_p(\mathbf{r})]$ part and the real $\mathrm{Re}[A_p(\mathbf{r})]$ part: $\varphi_p(\mathbf{r}) = \tan^{-1}\{\mathrm{Im}[A_p(\mathbf{r})]/\mathrm{Re}[A_p(\mathbf{r})]\}$. This corresponds to modeling of an ideal high-resolution wave-front sensor with a phase reconstructor. Because of the 2π periodicity of the function $\tan^{-1}$, the computed phase $\varphi_p(\mathbf{r})$ may contain 2π phase cuts (phase wraps) that were not removed prior to correction. At the points of the zero field $A_p(\mathbf{r}) = 0$, the phase $\varphi_p(\mathbf{r})$ can also contain branch points.

In actual phase-conjugation-type systems, the phase $\varphi_p(\mathbf{r})$ is reconstructed from wave-front sensor data and may also contain 2π phase cuts and branch points. Removal of the 2π phase cuts and branch points is computationally expensive and is not done in most adaptive systems operating with piston-type correctors.

Consider first an adaptive system with an ideal high-resolution Shack–Hartmann wave-front sensor capable of accurate reconstruction of the phase function $\varphi_p(\mathbf{r})$. The control signals $\{u_j\}$ in this case can be calculated by using deconvolution of the reconstructed phase function $\varphi_p(\mathbf{r})$ over the wave-front corrector influence function. For the piston-type corrector, this corresponds to

$$u_j = -\int_{\Omega_C} \varphi_p(\mathbf{r}) S_0(\mathbf{r} - \mathbf{r}_j) \mathrm{d}^2\mathbf{r} = -\int_{\Omega_j} \varphi_p(\mathbf{r}) \mathrm{d}^2\mathbf{r}, \tag{13}$$

where Ω_C and $\{\Omega_j\}$ are the corrector and its subaperture regions, respectively. The control signals in the phase-conjugation correction with a piston-type corrector can be computed by averaging the pupil-plane phase function $\varphi_p(\mathbf{r})$ over the subaperture areas $\{\Omega_j\}$.

The 2π phase cuts and branch points that are present inside some of the subapertures $\{\Omega_j^*\}$ ($j = 1,\ldots,N^*$) result in errors in computation of the control signal (13) in comparison with the corresponding control signal computations performed for the unwrapped phase with branch points removed. These errors are larger for low-resolution correctors with larger correcting element sizes d_c. Conversely, in the D-SPGD controller the control signals are calculated by using the sensor output signals $\bar{I}_j$ [see Eq. (1)] obtained by averaging the wave-front sensor intensity distribution over the correcting element subapertures. The 2π phase cuts do not affect the sensor output intensity distribution $I_\delta(\mathbf{r})$ and hence do not contribute additional errors as in the case of the phase-conjugation correction that uses phase reconstruction. The D-SPGD control algorithm is not the only one that does not require phase reconstruction. Among other algorithms of this type are SPGD,[35] gradient-flow,[15] and diffractive feedback (direct control).[44]

Note that in adaptive phase-conjugation-type systems the influence of 2π phase cuts on adaptation performance can be reduced if phase reconstruction is performed with sensor output signals $\bar{I}_j$ obtained by averaging the wave-front sensor intensity distribution over the correcting el-

ement subapertures first and performing the phase reconstruction afterward. This corresponds to adaptive system architecture with "matched" geometry of piston-type corrector and wave-front sensor photo-receiver arrays. In the case of an idealized interferometric-type sensor, the reconstructed phase can be calculated (in numerical simulations) by taking the arctangent of the ratio of the subaperture averaged real and imaginary parts of the received field complex amplitude.[16]

A comparison of D-SPGD and phase-conjugated correction system efficiency for different wave-front corrector resolutions is illustrated in Fig. 8 for a single distant phase screen and fixed D_c/r_0 ratio. The ensemble-averaged values of the metrics $\langle St \rangle$ and $\langle St_P \rangle$ achieved after 50 iterations of D-SPGD compensation (solid curves), after phase conjugation without the use of phase unwrapping (dotted curves), and after phase reconstruction of interferometric sensor data averaged over the subapertures (dotted–dashed curves) are shown as functions of the phase-screen location distance l. For a high-resolution adaptive system (e.g., corrector array with $N = 128 \times 128$ piston-type elements), the phase-conjugation compensation provides better performance, although the difference in the metric values is less than 5% when compared with the D-SPGD system. When corrector resolution is decreased, the D-SPGD controller provides better performance than the corresponding phase-conjugated control system based on averaging of phase over corrector subapertures and provides nearly the same performance by using first-interference-pattern averaging prior to phase reconstruction. The maximum difference in the values achieved for $\langle St \rangle$ and $\langle St_P \rangle$ in these two algorithms reaches 25% for $N = 8 \times 8$ and nearly 50% for $N = 4 \times 4$. Note that for $N > 8 \times 8$, the metric $\langle St_P \rangle$ in Fig. 8b increases when the distance l between the phase screen and the telescope pupil is increased (after the initial descent for $0 < l < 0.02 l_d$). This increase in $\langle St_P \rangle$ is related to the smoothing of intensity scintillations that occurs when the propagation distance between the single phase-distorting layer and the receiver aperture increases. This effect is absent in the case of multiple phase-distorting layers.

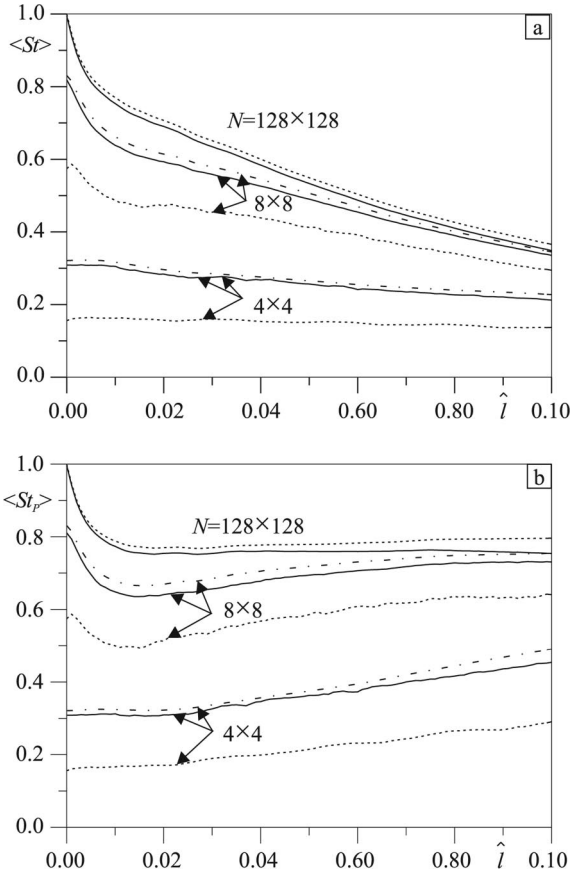

Fig. 8. Compensation of a single distant phase screen by use of the D-SPGD (solid curves) and phase conjugation (dotted curves), and phase reconstruction from interferometric sensor data averaged over the subaperatures (dotted–dashed curves) for different control channel numbers N (number of wave-front corrector actuators): a, Strehl ratio $\langle St \rangle$; b, the metric $\langle St_P \rangle$ versus the normalized propagation distance $\hat{l}$ for $D_c/r_0 = 8$.

G. Wave-front Corrector Position and Compensation Efficiency

In the preceding analysis we considered the most typical adaptive optical system arrangement, where the wave-front corrector is positioned in the image plane of the telescope pupil (conjugate pupil plane) as shown in Fig. 1. This preference in positioning the wave-front corrector is based on the commonly used assumption that the influence of optical inhomogeneties can be approximated by a single pupil-plane thin phase-distorting layer. Therefore these optical inhomogeneties can potentially be perfectly compensated by placing the corrector at the conjugate pupil plane. Note that full compensation is possible only if diffraction effects related to the finite aperture size of the optical relay system elements in Fig. 1 can be neglected.

In general, a wave-front corrector can be positioned at any plane if its size matches the beam size in the optical receiver system wave train. In the simplified system schematic in Fig. 9a, the corrector is positioned a distance l_C from the conjugate pupil plane formed by the lens L_1. Note that in Fig. 9a the distance l_C is positive for the corrector moved from the conjugate pupil plane ($l_C = 0$) toward the re-imaging lens L_1 and negative otherwise. For a single phase-screen arrangement, the distance $l_C = l_C^{\mathrm{ph}}$ corresponds to the corrector in the image (conjugate) plane of the distorting layer. For multiple distorting layers, the same distance $l_C = l_C^{\mathrm{ph}}$ corresponds to the plane conjugated to the most remote phase screen.

The questions raised are these: What is the effect of the corrector position on compensation efficiency? Where is the optimal position (distance l_C^{opt}) for the wave-front corrector for single or multiple distant phase-distorting layers?

Consider a single distant phase screen located a distance l from the telescope pupil, with the corrector displaced a distance l_C from the plane conjugate to the telescope pupil. Ignore aperture-induced diffraction effects by assuming an infinite aperture size for both the telescope L_R and the re-imaging lens L_1.

The dependence of the Strehl ratio $\langle St \rangle$ achieved after compensation process convergence on the normalized distance $\hat{l}_C = l_C/l_C^{\mathrm{ph}}$ is shown in Fig. 9b for both the high-resolution D-SPGD (solid curve) and the phase-conjugated (dotted curve) controllers. Note that

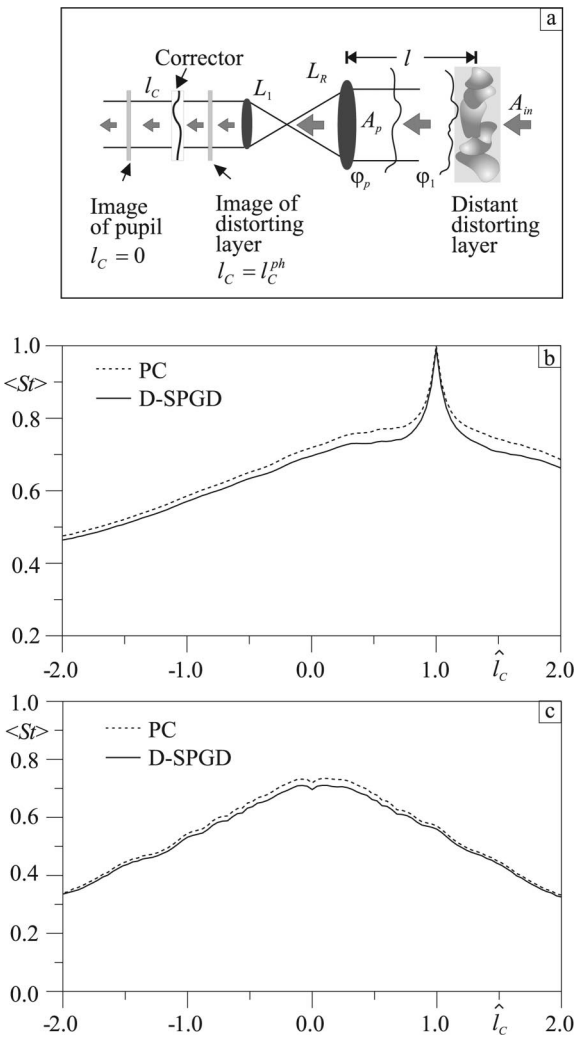

Fig. 9. Effect of the wave-front corrector position on phase-aberration compensation efficiency for a single distant phase screen located a distance $l = 0.05 l_d$ from the pupil plane with $D_c/r_0 = 8$: a, simplified schematic of the adaptive system optical train with the wave-front corrector positioned a distance l_C from the conjugate pupil plane; b, c, ensemble-averaged Strehl ratio $\langle St \rangle$ versus the normalized corrector displacement distance $\hat{l}_C = l_C/l_C^{\text{ph}}$ for high-resolution ($N = 128 \times 128$) D-SPGD (solid curves) and phase-conjugated (dotted curves) control algorithms for the receiver telescope with infinite aperture, b, and for the telescope having a finite aperture size of D_c coincident with the corrector aperture, c. The aperture radius of the input super-Gaussian beam $a = 1.5 D_c$.

compensation efficiency is estimated here by using the Strehl ratio $\langle St \rangle$ calculated for the optical wave at the corrector plane after phase compensation was performed. This corresponds to having the far-field sensor located at the plane conjugate to the corrector.

As expected, the Strehl ratio dependence has a sharp peak at the distance $\hat{l}_C = l_C/l_C^{\text{ph}} \approx 1$, with a maximum value of $\langle St \rangle \approx 1$ that corresponds to nearly perfect phase compensation and can be achieved only when aperture diffraction effects are neglected. Thus the optimal corrector position for both the phase-conjugation and D-SPGD adaptive optical systems is in the plane conjugate to the distorting layer plane ($l_C^{\text{opt}} \approx l_C^{\text{ph}}$). Relocating the wave-front corrector from this plane causes the pure phase modulation to transform into intensity scintillations at the corrector, followed by a sharp decrease in Strehl ratio.

As shown in Fig. 9b, the Strehl ratio achieved for D-SPGD system with the corrector at $l_C = 0$ (conjugate to the pupil-plane) is $\langle St \rangle \approx 0.70$. Note that compensation performance is nearly the same for both the high-resolution ($N = 128 \times 128$) phase conjugation and the D-SPGD controllers.

Next, consider compensation efficiency for a receiver telescope (lens L_R in Fig. 9a) with a finite aperture size of D_c. Assume that the telescope aperture coincides with the corrector aperture (after a corresponding scaling performed by the re-imaging lens L_1). The dependence of the ensemble-averaged Strehl ratio on the normalized corrector displacement from the conjugate pupil plane $\hat{l}_C$ is shown in Fig. 9c. The important difference from the infinite aperture case is the lack of the sharp peak in Fig. 9b corresponding to the corrector at the plane conjugate to the phase-distorting layer. The optimal corrector position corresponds to the wave-front corrector at the conjugate pupil plane ($l_C^{\text{opt}} \cong 0$).

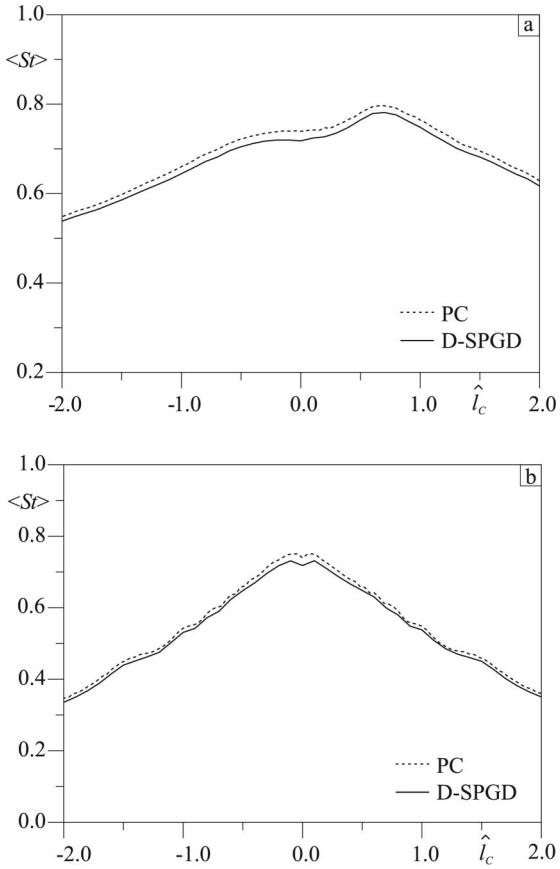

Fig. 10. Effect of wave-front corrector position on phase-aberration compensation efficiency for multiple phase screens equally spaced over the distance $l = 0.05 l_d$ ($D_c/r_0 = 8$): a, b, ensemble-averaged Strehl ratio $\langle St \rangle$ versus normalized displacement distance $\hat{l}_C = l_C/l_C^{\text{ph}}$ for high-resolution ($N = 128 \times 128$) D-SPGD (solid curves) and phase-conjugated (dotted curves) control algorithms for the receiver telescope with infinite aperture, a, and for the telescope aperture coincident with the corrector aperture of size D_c, b. The aperture radius of the input super-Gaussian beam $a = 1.5 D_c$.

The reason for such a change in optimal corrector position is telescope-aperture-induced diffraction leading to parasitic intensity and phase modulation of the optical field in the corrector area, which is not present for an infinite telescope with perfect imaging of the distorting layer at the corrector area. This aperture-induced parasitic phase modulation cannot be distinguished from the phase perturbations introduced by the distorting layer, and hence adaptive compensation results in Strehl ratio decrease. On the other hand, aperture diffraction effects do not affect the performance of a corrector positioned at the plane conjugate to the pupil plane (assuming that the re-imaging lens L_1 performs ideal imaging of the pupil plane). In the presence of aperture diffraction effects, the optimal corrector position coincides with the conjugate pupil plane.

Simulation results for multiple-distorting layers (ten phase screens equally spaced over the distance l) are presented in Fig. 10. For the infinite receiver aperture in Fig. 10a (no aperture diffraction), the optimal corrector position (maximum Strehl ratio value) corresponds to the distance $l_C^{\mathrm{opt}} \approx 0.75 l_C^{\mathrm{ph}}$. The maximum value of the Strehl ratio curve in Fig. 10a exceeds the achieved Strehl ratio value for the corrector placed at the conjugate pupil plane by less than 10%. For the single phase screen in Fig. 9a, this difference is almost 30% (compare Strehl ratio curves in Fig. 9b and Fig. 10a).

Any advantage that may arise from relocation of the wave-front corrector from the plane conjugate to pupil plane disappears in the presence of aperture diffraction effects (Fig. 10b). The Strehl ratio curves in this case have a well-defined maximum corresponding to a corrector located at the conjugate plane of the telescope pupil.

In addition, because in most cases the geometry of the location of the phase-distorting layers is unknown or known with some degree of uncertainty, the results presented here suggest that there is no compelling reason for relocating the wave-front corrector from the conjugate plane of the telescope pupil unless phase aberrations are the result of a single phase-distorting layer with an accurately defined location and aperture diffraction effects neglected.

5. CONCLUDING REMARKS

Propagation of optical waves (beams) through a continuously distributed or layered phase-distorting medium results in the development of intensity scintillations and phase singularities in the pupil of the optical receiver system. Both effects are highly undesirable for the traditional (based on phase conjugation) adaptive optics technique, which requires direct reconstruction of the phase-aberration function on the basis of data obtained from a wave-front sensor. The intensity scintillations "propagate" to the wave-front sensor output, resulting in a parasitic modulation of the sensor's output and phase-reconstruction errors. Wave-front phase singularities (branch points) add more complexity to phase reconstruction computations.

In the analysis presented here we considered an alternative to the phase-conjugation control strategy—wave-front control based on a decoupled stochastic parallel gradient descent (D-SPGD) technique originally introduced for compensation of pupil-plane phase aberrations.[35] This technique does not require reconstruction of the phase and as demonstrated above is more robust to intensity scintillations. The piston-type wave-front corrector in the adaptive optics system considered here performs better in compensation of phase aberrations containing branch-points and 2π phase cuts than modal-type correctors (e.g., continuously deformable mirrors).

Comparative analysis of D-SPGD and phase-conjugation control shows that the two adaptive optics system architectures achieve nearly the same compensation levels for high-resolution systems, but the D-SPGD control algorithm is more efficient for low-resolution controls (if 2π phase cuts and branch points are not initially removed from the reconstructed phase).

Analysis also shows that with a single distant phase-distorting layer, the achieved gain in compensation performance with use of an adaptive optics system of higher spatial resolution (larger number of wave-front corrector actuators) decreases when the distance between the receiver aperture and the distorting layer increases.

Optimization of adaptive compensation efficiency includes not only optimization of control algorithm parameters but also identification of the optimal position for the wave-front corrector in the adaptive system wave train. The recipe widely used in the multiconjugate adaptive optics approach for wave-front corrector position suggests positioning the wave-front corrector in the conjugate (image) plane of the phase-distorting layer that the corrector is intended to compensate. As shown in the presented analysis, this recipe indeed results in optimal closed-loop compensation performance, but only if aperture-induced diffraction effects can be neglected. In the presence of aperture-induced diffraction or for the case of multiple phase-distorting layers separated by short distances, the optimal corrector position for both closed-loop phase conjugation and D-SPGD control algorithms corresponds to the conjugate pupil plane.

The results of numerical simulations presented here are only for an on-axis wave (wave propagating along the optical axis), which corresponds to a narrow-field-of-view adaptive receiver system. This restriction is removed in Part II (this issue), in which we analyze wide-field-of-view adaptive closed-loop control.

ACKNOWLEDGMENTS

This work was supported by the U.S. Joint Technology Office under contract JTO-02-602-18 and by the Collaborative Technology Alliance under University of Maryland contract ATS-01-4-32430.

REFERENCES

1. H. W. Babcock, "The possibility of compensating astronomical seeing," Publ. Astron. Soc. Pac. **65**, 229–236 (1953).
2. J. W. Hardy, *Adaptive Optics for Astronomical Telescopes* (Oxford U. Press, New York, 1998).
3. F. Roddier, *Adaptive Optics in Astronomy* (Cambridge U. Press, New York, 1999).
4. M. C. Roggemann and B. M. Welsh, *Imaging through Turbulence* (CRC Press, New York, 1998).

5. L. Sherman, J. Y. Ye, O. Albert, and T. B. Norris, "Adaptive correction of depth-induced aberrations in multiphoton scanning microscopy using a deformable mirror," J. Microsc. (Oxford) **206**, 65–71 (2002).
6. P. Artal, S. Marcos, R. Navarro, and D. Williams, "Odd aberrations and double-pass measurements of retinal image quality," J. Opt. Soc. Am. A **12**, 195–201 (1995).
7. D. L. Fried and J. L. Vaughn, "Branch cuts in the phase function," Appl. Opt. **31**, 2865–2882 (1992).
8. D. L. Fried, "Branch point problem in adaptive optics," J. Opt. Soc. Am. A **15**, 2759–2768 (1998).
9. E. O. LeBigot and W. J. Wild, "Theory of branch-point detection and its implementation," J. Opt. Soc. Am. A **16**, 1724–1729 (1999).
10. M. C. Roggemann and A. C. Koivunen, "Branch-point reconstruction in laser beam projection through turbulence with finite-degree-of-freedom phase-only wave-front correction," J. Opt. Soc. Am. A **17**, 53–62 (2000).
11. V. Aksenov, V. Banakh, and O. Tikhomirova, "Potential and vortex features of optical speckle fields and visualization of wave-front singularities," Appl. Opt. **37**, 4536–4540 (1998).
12. M. C. Roggemann and D. J. Lee, "Two-deformable-mirror concept for correcting scintillation effects in laser beam projection through the turbulent atmosphere," Appl. Opt. **37**, 4577–4585 (1998).
13. J. D. Barchers, "Evaluation of impact of finite-resolution effects on scintillation compensation using two deformable mirrors," J. Opt. Soc. Am. A **18**, 3098–3109 (2001).
14. M. A. Vorontsov, E. W. Justh, and L. A. Beresnev, "Adaptive optics with advanced phase-contrast techniques. I. High-resolution wave-front sensing," J. Opt. Soc. Am. A **18**, 1289–1299 (2001).
15. E. W. Just, M. A. Vorontsov, G. W. Carhart, L. A. Beresnev, and P. S. Krishnaprasad, "Adaptive optics with advanced phase-contrast techniques. II. High-resolution wave-front control," J. Opt. Soc. Am. A **18**, 1300–1311 (2001).
16. J. D. Barchers, "Closed-loop stable control of two deformable mirrors for compensation of amplitude and phase fluctuations," J. Opt. Soc. Am. A **19**, 926–945 (2002).
17. J. M. Beckers, "Detailed compensation of atmospheric seeing using multi-conjugate adaptive optics," F. J. Roddier, ed., Proc. SPIE **1114**, 215–217 (1989).
18. N. Ageorges and C. Dainty, *Laser Guide Star Adaptive Optics for Astronomy* (Kluwer Academic, Dordrecht, London, 2000).
19. D. C. Johnston and B. M. Welsh, "Analysis of multiconjugate adaptive optics," J. Opt. Soc. Am. A **11**, 394–408 (1994).
20. B. L. Ellerbroek, C. Van Loan, N. P. Pitsianis, and R. J. Plemmons, "Optimizing closed-loop adaptive-optics performance with use of multiple control bandwidths," J. Opt. Soc. Am. A **11**, 2871–2886 (1994).
21. J. D. Barchers and B. L. Ellerbroek, "Improved compensation of turbulence-induced amplitude and phase distortions by means of multiple near-field phase adjustments," J. Opt. Soc. Am. A **18**, 399–411 (2001).
22. B. L. Ellerbroek and F. Rigaut, "Methods for correcting tilt anisoplanatism in laser-guide-star-based multiconjugate adaptive optics," J. Opt. Soc. Am. A **18**, 2539–2547 (2001).
23. C. Flicker, "Sequence of phase correction in multi-conjugate adaptive optics," Opt. Lett. **26**, 1743–1745 (2001).
24. A. Tokovinin, M. Le Louarn, and M. Sarazin, "Isoplanatism in multi-conjugate adaptive optics systems," J. Opt. Soc. Am. A **17**, 1819–1827 (2000).
25. R. Ragazzoni, E. Marchetti, and F. Rigaut, "Modal tomography for adaptive optics," Astron. Astrophys. **342**, L53–L56 (1999).
26. R. A. Muller and A. Buffington, "Real-time correction of atmospherically degraded telescope images through image sharpening," J. Opt. Soc. Am. **64**, 1200–1210 (1974).
27. M. A. Vorontsov and V. I. Shmalhauzen, *Principles of Adaptive Optics* (Nauka, Moscow, 1985).
28. T. R. O'Meara, "The multi-dither principle in adaptive optics," J. Opt. Soc. Am. **67**, 306–315 (1977).
29. M. A. Vorontsov, G. W. Carhart, D. V. Pruidze, J. C. Ricklin, and D. G. Voelz, "Adaptive imaging system for phase-distorted extended source/multiple distance objects," Appl. Opt. **36**, 3319–3328 (1997).
30. M. A. Vorontsov and V. P. Sivokon, "Stochastic parallel-gradient-descent technique for high-resolution wave-front phase-distortion correction," J. Opt. Soc. Am. A **15**, 2745–2758 (1998).
31. M. A. Vorontsov, G. W. Garhart, M. Cohen, and G. Cauwenberghs, "Adaptive optics based on analog parallel stochastic optimization: analysis and experimental demonstration," J. Opt. Soc. Am. A **17**, 1440–1453 (2000).
32. E. Zeek, K. Maginnis, S. Backus, U. Russek, M. Murnane, G. Mourou, H. Kapteyn, and G. Vdovin, "Pulse compensation by use of deformable mirrors," Opt. Lett. **24**, 493–495 (1999).
33. L. Arnold, "Optimized axial support topologies for thin telescope mirrors," Opt. Eng. **34**, 567–574 (1995).
34. S. S. Chesnokov and I. V. Davletshina, "Simplex method in problems of light-beam phase control," Appl. Opt. **34**, 8375–8381 (1995).
35. M. A. Vorontsov, "Decoupled stochastic parallel gradient descent optimization for adaptive optics: integrated approach for wave-front sensor information fusion," J. Opt. Soc. Am. A **19**, 356–368 (2002).
36. R. N. Smartt and W. H. Steel, "Theory and application of point-diffraction interferometers," Jpn. J. Appl. Phys. **14**, 351–356 (1975).
37. P. Hariharan, *Selected Papers on Interferometry* (SPIE Optical Engineering Press, Bellingham, Wash., 1991).
38. S. M. Rytov, Yu. A. Kravtsov, and V. I. Tatarskii, *Principles of Statistical Radiophysics 4, Wave Propagation through Random Media* (Springer-Verlag, Berlin, 1989).
39. R. Q. Fugate, D. L. Fried, G. A. Ameer, B. R. Boeke, S. L. Browne, P. H. Roberts, R. E. Ruane, G. A. Tyler, and L. M. Wopat, "Measurement of atmospheric wave-front distortion using scattered light from a laser guide-star," Nature **353**, 144–146 (1991).
40. L. C. Andrews, "An analytic model for the refractive index power spectrum and its application to optical scintillations in the atmosphere," J. Mod. Opt. **39**, 1849–1853 (1992).
41. D. L. Fried, "Statistics of a geometric representation of wave-front distortion," J. Opt. Soc. Am. **55**, 1427–1435 (1965).
42. A. T. Young, "Aperture filtering and saturation of scintillation," J. Opt. Soc. Am. **60**, 248–250 (1970).
43. J. D. Barchers and D. L. Fried, "Optimal control of laser beams for propagation through a turbulent medium," J. Opt. Soc. Am. A **19**, 1779–1793 (2002).
44. V. P. Sivokon and M. A. Vorontsov, "High-resolution adaptive phase distortion suppression based solely on intensity information," J. Opt. Soc. Am. A **16**, 2567–2573 (1999).